near the back focal plane of lens f2. The first relay lens f2 forms an image of the fiber facet at the back focal plane of the second relay lens f3, which recollimates the beam onto the objective. The objective is a distance f3 from the second relay lens such that the scanned beam pivots about the center of the objective. The objective is a 30x, 0.9 NA water immersion objective designed for NIR wavelengths with a working distance of 1.3 mm.

The reference arm uses a reflective geometry grating phase delay line. The beam from the fiber collimator is directed onto a 36.152 l/mm grating which diffracts the beam onto a f = 5 cm curved mirror, one focal length from the grating. The curved mirror, in turn focuses the spectrally dispersed beam back onto a 12 mm width galvonometer controlled mirror which is displaced in the horizontal direction. The galvo mirror can be tilted to produce an inclined phase versus wavelength in the focal plane of the spectrally dispersed beam.

The pivot axis of the mirror can be offset to produce independent control of phase and group delay and is set to produce a phase modulation only. The mirror angle is scanned with a triangle waveform at 500 Hz to provide 1000 forward and backward scans per second and a phase ramp modulation corresponding to a 900 kHz heterodyne frequency.

The XY galvo mirrors in the hand held probe are scanned in a raster pattern. The fast axis mirror is also scanned at 500 Hz and synchronized with the phase modulation scan. The slow axis mirror is scanned at 2 to 4 frames per second to acquire 500 to 250 image lines. The output of the interferometer is detected and demodulated with a log demodulator similar to that used in OCT. The demodulated output is digitized with a 5 MHz, 12 bit A/D converter and displayed on the computer. The images can be saved in digital form as well as in video using an S-VHS recorder.

Results

Figure 2 shows en face OCM images where the reference arm group delay is set to match the confocal plane of the imaging probe. The resolution of the system was tested by imaging an Air Force resolution chart (Fig. 2a) and a 300 lp/mm diffraction grating (Fig. 2b). The system could resolve the smallest 4.4 um elements of the chart and diffraction grating lines of 3.3 um. Furthermore, it was possible to resolve smaller surface features on the targets, demonstrating transverse image resolutions better than 3.3 um. The field of view is approximately 130 um by 140 um and the image plane was relatively flat over this range.
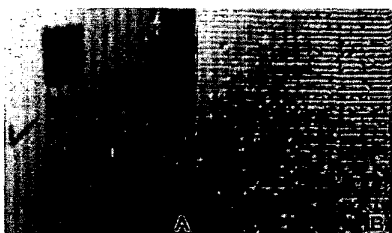

CWC2 Fig. 2. Examples of optical coherence microscopy en face images of an Air Force resolution chart (A) and a diffraction grating (B). The images are 130 um by 140 um and demonstrate a transverse resolution of better than 3.3 um.

To investigate imaging in a biological system, *in vivo* OCM imaging was performed on an African frog tadpole (*Xenopus laevis*). The tadpole was imaged from the dorsal side with 1375 × 500 and 1375 × 250 pixel resolutions at 2 to 4 frames per second, respectively (Fig. 3). Cellular structure was clearly visible at multiple en face imaging depths. The cell nuclei and cell borders appear highly scattering. In addition, circulatory flow in a large vessel was also visible in sequential images or video. To demonstrate materials imaging, OCM imaging was performed on laser fabricated optical waveguides in glass. The waveguides are inside the glass and normally require phase contrast microscopy for visualization.

Preliminary studies have also been performed at 800 nm and the phase modulation has been demonstrated with over 130 nm of bandwidth. This paper will report high resolution, high speed OCM imaging results at both 1300 nm and 800 nm wavelengths.

References

1. D. Huang, E. Swanson, C.P. Lin C, J.S. Schuman, W.G. Stinson, W. Chang, M.R. Hee, T. Flotte, K. Gregory, C.A. Puliafito, J.G. Fujimoto. "Optical coherence tomography," Science, 254, 1178–1181 (1991).
2. J.A. Izatt, M.R. Hee, G.M. Owen, E.A. Swanson, and J.G. Fujimoto, "Optical coherence microscopy in scattering media," Opt. Lett. 19, 590–592 (1994).
3. M. Rajadhyaksha, S. Gonzalez, J.M. Zavislan, R.R. Anderson, R.H. Webb, "in vivo Confocal Scanning Laser Microscopy of Human Skin II: Advances in Instrumentation and Comparison With Histology," J. of Invest. Derm., 113, 293 (1999).
4. V. Westphal, H.-W. Wang, J.A. Izatt, "Real-time in vivo optical coherence microscopy," CLEO 2001 Digest pg. 331–332.
5. G.J. Tearney, B.E. Bouma, and J.G. Fujimoto, "High-speed phase- and group-delay scanning with a grating-based phase control delay line," Opt. Lett. 22, 1811–1813, (1997).
6. J.P. Heritage, A.M. Weiner, R.N. Thurston, "Picosecond pulse shaping by spectral phase and amplitude manipulation" Opt. Lett. 10, 609–611 (1985).
7. A.V. Zvyagin, D.D. Sampson, "Achromatic optical phase shifter-modulator," Opt. Lett. 26, 187–190 (2001).
8. B.E. Lemoff and C.P.J. Barty, "Quintic phase limited, spatially uniform expansion and re-
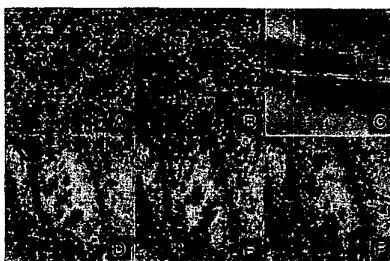
CWC2 Fig. 3. OCM en face images taken of *Xenopus laevis* tadpole and of a laser-fabricated waveguide embedded in glass (C). Images A, D-E are 1375 × 250 pixels taken at 4 frames per second, while images B and C are 1375 × 500 pixels taken at 2 frames per second. The field of view in the images is 130 um × 140 um.

compression of ultrashort optical pulses," Opt. Lett. 18, 1651–1653 (1993).

CWC3 **Invited** **3:00 pm**

Near-Infrared Detection of Correlated Activity in the Brain

Enrico Gratton, Laboratory for Fluorescence Dynamics, University of Illinois at Urbana-Champaihn

Since the introduction of the fMRI technique few years ago functional studies of the brain capable of good localization are now relatively common. One major drawback of the fMRI method is that the BOLD effect, which is at the basis of the method, is sensitive to changes in blood flow and volume rather than to neuronal activity. Furthermore, fMRI has not yet reached the necessary temporal resolution to follow the rapid changes due to neuronal activation. Near-ir light can pass trough the skull and reach the surface of the brain. It is well established in exposed cortex experiments that brain activity changes the brain surface optical properties in the near-ir, due both to changes in blood flow and to scattering from the brain cells. Several researches have proposed optical methods and the near-ir spectral region to measure brain function non-invasively with high temporal resolution and good localization. While the detection of slow (in the second time scale) changes of blood flow by the near-ir method is well-proven, the detection of optical changes associated with fast (in the 10–100 ms) neuronal signal has been a relatively small field practiced by few experts. Our research has shown that it is possible to increase by at least one order of magnitude the detection of the small changes associated with neuronal activity. Our technical developments and a new sensor could make this optical technique widely available and complementary to fMRI.

CWC4 **3:30 pm**

Polarization-gated Imaging Techniques Based on Time-resolved Stokes Vectors for Filament Tissues

Chia-Wei Sun, C.C. Yang, and Yean-Woei Kiang, Department of Electrical Engineering, Graduate Institute of Electro-Optical Engineering, and Graduate Institute of Communication Engineering, National Taiwan University, 1, Roosevelt Road, Sec. 4, Taipei, Taiwan, R.O.C., Email: ccy@cc.ee.ntu.edu.tw

Long-Sheng Lu and Chii-Wann Lin, Department of Pharmacology and Graduate Institute of Bioengineering, National Taiwan University, 1, Roosevelt Road, Sec. 4, Taipei, Taiwan, R.O.C.

Xueding Wang and Lihong V. Wang, Optical Imaging Laboratory, Biomedical Engineering Program, Texas A&M University, 3210 TAMU, College Station, Texas, U.S.A.

Biomedical imaging operation based on snake photons via time gating techniques, combined with polarization discrimination, has been proved useful for medical diagnosis. The polarization discrimination method is usually quite effective in tissues of statistically isotropic structures, which cause strong depolarization effects.

However, in tissues with filament structures, such a technique becomes less effective due to the coherent polarization evolution in the tissue.[1] In this paper, we report the discovery of using various time-resolved Stokes vector components for more efficient imaging of filament tissues. In particular, the Stokes vector components S2 and S3 were found more useful, compared with the other two components. The time-resolved Stokes vectors of signals transmitting chicken breast tissue, mouse cardiac muscle tissue, and polystyrene micro-sphere solution will be compared. A target of chicken bone in chicken breast tissue is used for demonstrating the effectiveness of various Stokes vector components for imaging purpose. Also, Monte Carlo simulations were conducted for comparison.[2]

In our experiments, a mode-locked Ti:sapphire laser provided 100 fsec pulses at 800 nm. The input and output polarization states were controlled with polarizers and waveplates. The transmitted signals of samples were directed to a streak camera with a fiber bundle. Fig. 1(a) shows the experimental data of time-resolved Stokes vectors after signal transmission through a 0.38 μm polystyrene micro-sphere solution diluted to 0.066% concentration. The numbers of the x-axis indicate the sixteen components of the Stokes vectors with various input polarization states of 0, 45, 90 degrees with respect to the filament direction, and circular polarization. The y-axis represents the temporal scale (psec) and the z-axis shows the relative intensity of those components. The Monte Carlo algorithm, which is based on
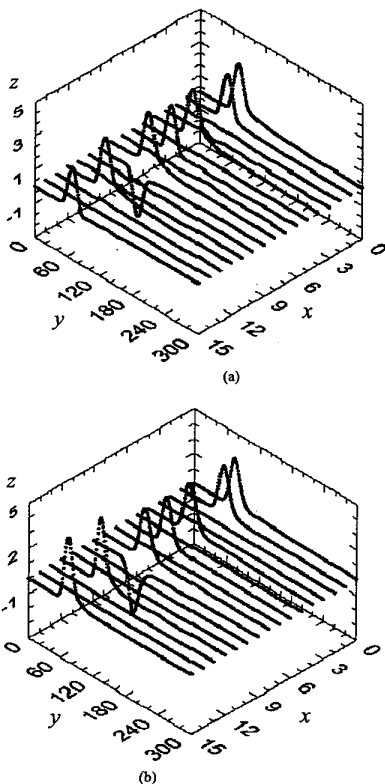
multiple scattering events of the radiative theory, provides the results in Fig. 1(b) under the same conditions. Very consistent curves with experimental data can be seen.

Fig. 2(a) shows the time-resolved Stokes vector with input linear polarization parallel to tissue filaments after passing through 2-cm thick chicken breast tissue. Fig. 2(b) shows the counterpart when a thin bone of 1.6 mm sticking into the breast tissue. Although the two sets of results look alike, their snake photon parts are quite different. Figs. 3(a) and (b) show the close-ups of Figs. 2(a) and (b) around the rise of the curves, respectively. The comparison between Figs 3(a) and (b) indicates that S0 and S1 are almost the same while S2 and S3 are quite different. Conventionally, S1 was

(a)

(b)
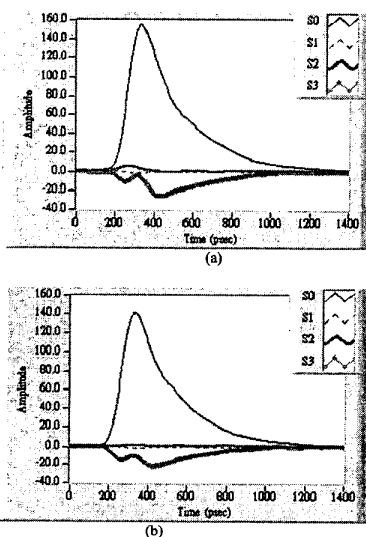
CWC4 **Fig. 2.** (a) Experimental Stokes vector results with linear polarization input parallel with filaments of chicken breast tissue. (b) Experimental Stokes vector results with linear polarization input when a bone sticking into the chicken breast tissue.

(a)

(b)
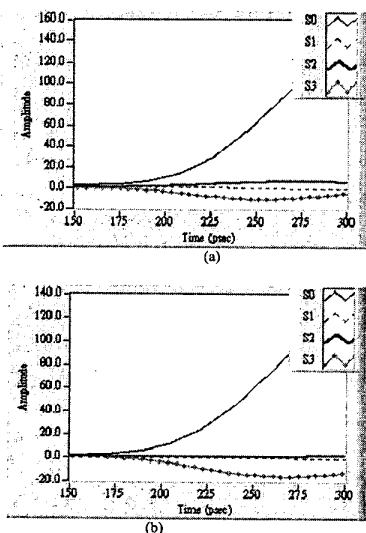
CWC4 **Fig. 3.** Snake photon parts of Stokes vectors in Figs. 2(a) and (b).

used for polarization-gating imaging operation. It is ineffective as further evidenced with the results here. However, the significant differences in S2 and S3 should lead to effective imaging operation. In other words, with 45 degrees linear polarization and circular polarization output monitoring, we should be able to obtain better-quality images. We applied such operations to the diagnosis of abnormal cardiac muscle, especially in atrioventricular block and myocarditis. Such results will be presented.

References

1. C.W. Sun, C.Y. Wang, C.C. Yang, Y.W. Kiang, I.J. Hsu, and C.W. Lin, "Polarization gating in ultrafast-optics imaging of skeletal muscle tissue," Optics Letter 26, 432 (2001).
2. X. Wang and L.V. Wang, "Propagation of polarized light in birefringent turbid media: time-resolved simulations," Optics Express 9, 254.

CWC5   3:45 pm

Spectrally Resolved TCSPC FRET Imaging

Wolfgang Becker, Axel Bergmann, Becker & Hickl GmbH, Nahmitzer Damm 30, D-12277 Berlin, Germany, Email: info@becker-hickl.com

Klaus Benndorf, Christoph Biskup, Thomas Zimmer, Friedrich-Schiller-University, Institute of Physiology II, D-07740 Jena, Germany, Email: cbis@mti-n.uni.jena.de

1. Instrumentation

The setup consists of an LSM-510-NLO microscope (Zeiss), a PML-16 16 channel PMT detector head with a polychromator and an SPC-730 time-correlated single photon counting (TCSPC) imaging module (Becker & Hickl). The principle of the TCSPC imaging technique is shown in fig. 1.

For each photon, the 16 channel detector head delivers a timing pulse and a number that indicates in which channel the photon was detected. The SPC-730 module measures the time between this timing pulse and the next laser pulse, receives the detector channel number, and determines the X/Y coordinates of the laser beam in the scanning area. This information is used to build up a four-dimensional histogram of the photon density over the time, the wavelength, and the image coordinates. The result is a set of 16 image stacks for different wavelengths. Each stack contains 64 images for subsequent times after the excitation.

2. Results

Fig. 2 shows an HEK cell expressing a hybrid protein in which CFP and YFP are linked together by a short peptide of 6 amino acids. The image was obtained by summing the photons from all time channels of the CFP fluorescence. Fluorescence decay analysis in a selected region reveals a double exponential decay both for CFP and YFP. The intensity coefficient of the fast component is positive for CFP and negative for YFP, indicating that energy is transferred from CFP to YFP.

While the lifetime of the fast decay component is a measure of the distance of the FRET partners the ratio of the intensity coefficients of the decay components is an indicator of the fraction of molecules participating in the FRET. Fig. 3 contains the intensity as brightness and the ratio of the coefficients as colour. The results are shown for the CFP and the YFP fluorescence. Due to the

(a)

(b)

CWC4 **Fig. 1.** (a) Experimental Stokes vector results in 0.38 μm polystyrene micro-spheres solution diluted to 0.066% concentration. (b) Simulated Stokes vector results.